Research Square

Preprints are preliminary reports that have not undergone peer review.
They should not be considered conclusive, used to inform clinical practice,
or referenced by the media as validated information.

Combined Use of Gallium and a Composite Cross-Linked Binder to Improve Silicon Anode Performance

Entian Fang
Kunming University of Science and Technology
Junkai Li
Kunming University of Science and Technology
Kaizhao Wang
kaizhao_wang@kust.edu.cn

Kunming University of Science and Technology
Hongrui Wang
Kunming University of Science and Technology
Taotao Wang
Kunming University of Science and Technology
Jin Hu
Kunming University of Science and Technology

Research Article

Keywords: Silicon anodes, Gallium, Cross-linked binders, Cycling stability, Lithium-ion batteries

Posted Date: November 25th, 2026

DOI: https://doi.org/10.21203/rs.3.rs-11320444/v1

License: This work is licensed under a Creative Commons Attribution 4.0 International License.
Read Full License

Additional Declarations: No competing interests reported.

Combined Use of Gallium and a Composite Cross-Linked Binder to Improve Silicon Anode Performance

EnTian Fang[1], Junkai Li[1,2], Kaizhao Wang[1]*, Hongrui Wang[1], Taotao Wang[1], Jin Hu[1]*

1. Faculty of Materials Science and Engineering, Kunming University of Science and Technology, Kunming, 650093, China

2. State Key Laboratory of Complex Nonferrous Metal Resources Clean Utilization, College of Metallurgy and Energy Engineering, Kunming University of Science and Technology, Kunming 650093, China

E-mail address: kaizhao_wang@kust.edu.cn (K. Wang); hujin@kmust.edu.cn (J. Hu)

ABSTRACT

Silicon anodes offer high theoretical capacity, but large volume changes during cycling compromise electrode integrity and capacity retention. Here, a silicon/gallium composite anode incorporating a poly(vinyl alcohol)/sodium alginate (PVA/SA) binder was evaluated against silicon/carbon reference electrodes in lithium-metal half cells. The Si/Ga–PVA/SA electrode delivered 1679.37 mAh g^{-1} after 200 cycles at 0.5 A g^{-1}, retaining 71.7% of its initial capacity, compared with 33.0% for Si/C–PVA/SA and 5.7% for Si/C–PVDF. Post-cycling microscopy revealed a more continuous electrode structure and less coating thickening in the Ga-containing formulation. Lower interfacial impedance and improved electrolyte wettability further accompanied its enhanced electrochemical performance. These findings support the combined use of Ga and a functional PVA/SA binder as a strategy for improving silicon electrode stability.

KEYWORDS：
Silicon anodes; Gallium; Cross-linked binders; Cycling stability; Lithium-ion batteries

1 INTRODUCTION

The growing demand for electric vehicles, portable electronics, and renewable energy storage has driven the development of lithium-ion batteries (LIBs) with higher energy density and longer service life. Although graphite remains the predominant anode material in commercial LIBs, its theoretical specific capacity of 372 mAh g^{-1} limits further improvements in anode capacity[1,2,3]. Silicon (Si) is therefore an attractive candidate for next-generation anodes because of its high theoretical lithium-storage capacity, low lithiation potential, natural abundance, and relatively low cost. These advantages offer considerable potential for increasing battery energy density. Realizing this potential, however, requires electrode architectures that can sustain reversible lithium storage while maintaining structural integrity and effective charge transport over prolonged cycling[4].

The principal challenge facing Si anodes is the large volume change associated with repeated lithiation and delithiation, which can reach approximately 300%, depending on the lithiation endpoint[5,6]. The resulting stresses can fracture Si particles, weaken their adhesion to the current collector, and disrupt electrical contact within the electrode. Meanwhile, repeated expansion and contraction can rupture the solid electrolyte interphase (SEI), exposing fresh surfaces to the electrolyte and promoting further interphase formation. These coupled processes consume electrolyte and cyclable lithium, increase interfacial impedance, and progressively isolate active material, leading to irreversible capacity loss and poor cycling stability[7]. Consequently, improving Si anodes requires more than increasing their initial conductivity: conductive pathways and interfacial adhesion must also be maintained as the electrode undergoes substantial dimensional changes[8].

Considerable efforts have been devoted to addressing these challenges through nanostructuring, porous architecture design, carbon coating, alloying, and the development of functional polymeric binders. Among these approaches, silicon/carbon

(Si/C) composites have attracted particular attention because of their ability to combine lithium-storage capacity with improved electronic conductivity[9]. Carbon matrices, including graphene, carbon nanotubes, porous carbon, and amorphous carbon, can disperse Si particles, provide conductive pathways, and create space for expansion. Nevertheless, their effectiveness depends on both the mechanical stability of the framework and the accessibility of Si to the electrolyte[10]. Repeated deformation can still disrupt Si–carbon contacts, while increasing the carbon fraction to improve structural stability dilutes the contribution of high-capacity Si to the composite[11]. The binder introduces a further constraint. Conventional poly(vinylidene fluoride) (PVDF) formulations may provide insufficient adhesion and stress accommodation for highly expanding Si electrodes, allowing cracks and particle detachment to develop during cycling. These limitations motivate the combined design of conductive components and binders that can preserve electrical contact while accommodating mechanical deformation[12,13,14].

Gallium (Ga) offers a potentially useful conductive component for this purpose because it combines high electronic conductivity with a low melting point of approximately 29.8 °C. When present in the liquid state, Ga can redistribute around adjacent particles, providing a possible means of maintaining contact as the electrode structure evolves[15]. Unlike an entirely passive conductive additive, Ga can also participate in reversible alloying and dealloying with lithium. The accompanying changes in phase composition and interfacial contact may therefore influence both charge storage and electrode transport[16]. If Ga is regenerated in a liquid state during delithiation, its redistribution could help reconnect locally separated particles and accommodate deformation. This possibility provides a rationale for incorporating Ga into Si electrodes, although the extent of such behavior depends on the operating temperature, thermal history, and electrochemical state. Its high electronic conductivity further supports its use as an alternative conductive phase, while its effects on interfacial transport must be assessed within the composite electrode[17].

The effectiveness of a Ga-containing conductive phase also depends on the surrounding binder matrix. A suitable binder should maintain particle cohesion and

adhesion while allowing sufficient compliance to accommodate Si expansion. Sodium alginate (SA) and poly(vinyl alcohol) (PVA) offer complementary functionalities in this respect[18]. The carboxylate and hydroxyl groups of SA can participate in polar interactions with oxidized Si surfaces, whereas the hydroxyl-rich, flexible PVA chains provide film-forming ability and additional intermolecular interactions. Introducing borax into the PVA/SA system provides a route to borate-mediated cross-linking alongside hydrogen bonding, with the aim of improving cohesion without eliminating polymer flexibility[19]. Combining this binder with Ga thus offers a design in which the polymer network supports the particle assembly while the conductive phase may accommodate changes in local contact. The central question is whether these complementary functions can translate into improved structural retention and electrochemical performance during repeated cycling. Addressing this question requires evaluating morphology, conductivity, and electrochemical behavior together, rather than inferring electrode stability from the properties of the individual components alone[20].

Here, we investigate a Si/Ga–PVA/SA composite anode prepared by incorporating Ga and commercial nanosilicon into a borax-cross-linked PVA/SA binder through a straightforward slurry-processing route. The fabrication avoids high-temperature carbon coating and vapor-phase deposition, allowing the proposed combination to be examined using conventional electrode preparation methods. Si/C–PVA/SA and Si/C–PVDF electrodes serve as reference formulations for assessing the effects of replacing the conductive component and changing the binder system. Structural and surface characterization, conductivity measurements, and post-cycling microscopy are combined with cycling, rate, and electrochemical kinetic analyses to examine how the formulation affects electrode integrity and lithium-storage behavior. The Ga-containing electrode exhibits improved capacity retention and a more continuous post-cycling morphology under the tested half-cell conditions. These findings support the combined use of Ga and a functional polymer binder as a strategy for improving Si electrode stability and provide a basis for further examination of the proposed interfacial accommodation mechanism.

2 RESULTS AND DISCUSSION

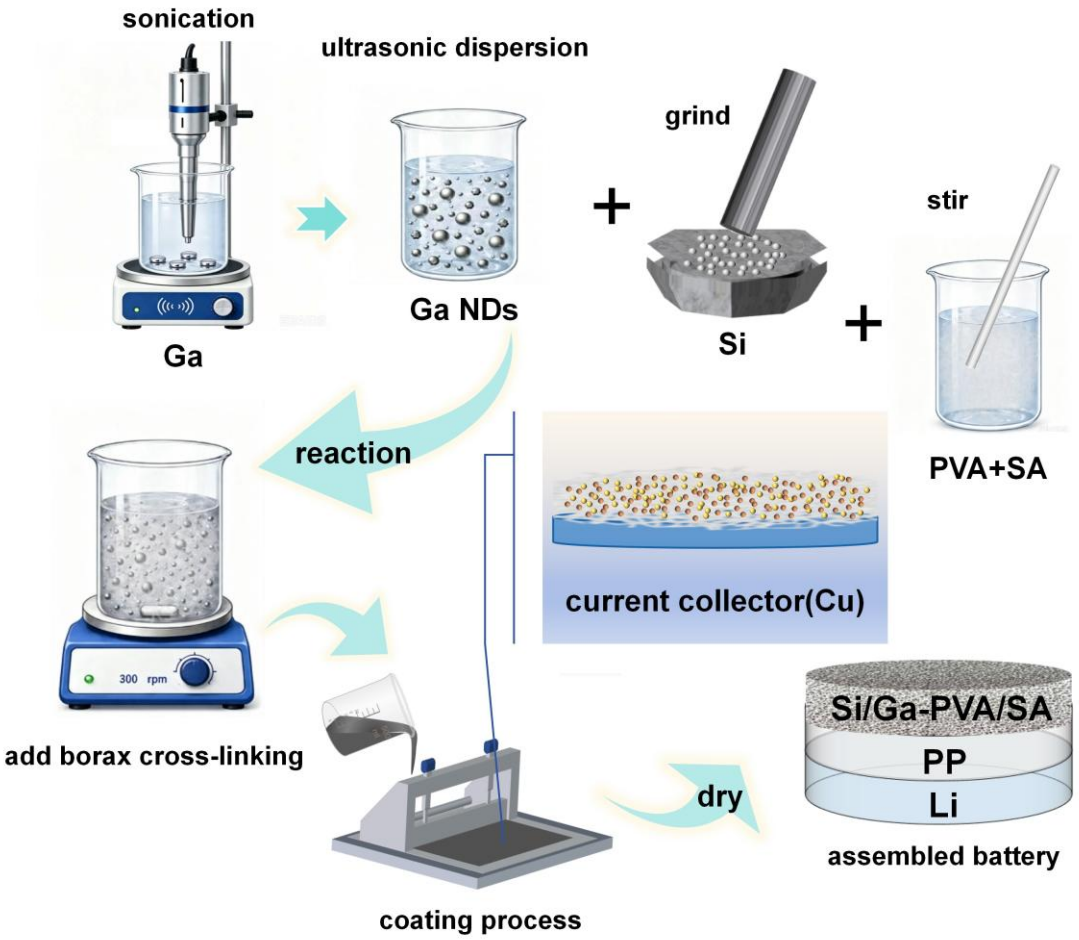

Fig.1 Schematic diagram of the synthesis process for Si/Ga composite anodes

Figure 1 illustrates the fabrication process and proposed structural design of the Si/Ga–PVA/SA composite anode. Ga was first dispersed in an aqueous solution containing sodium alginate (SA) and poly(vinyl alcohol) (PVA) by ultrasonication. Commercial nanosilicon particles with an average diameter of approximately 100 nm were subsequently introduced, followed by the addition of borax to promote cross-linking within the binder matrix. After stirring, the resulting slurry was cast onto a copper current collector and dried to obtain the composite electrode. Detailed preparation procedures are provided in the Supporting Information. This process incorporated Si and Ga into a common polymer matrix, combining a conductive, electrochemically active Ga phase with a binder network designed to maintain particle cohesion and interfacial adhesion.

The proposed roles of the individual components are complementary. Carboxylate and hydroxyl groups in SA can participate in polar interactions and hydrogen bonding with hydroxylated Si surfaces, potentially strengthening particle–binder adhesion[21]. The hydroxyl-rich, flexible PVA chains provide film-forming capability and additional intermolecular interactions, while borax-mediated cross-linking is intended to reinforce binder cohesion[22,23]. Together, these interactions could help distribute local stresses and limit particle separation during cycling. The Ga phase provides an additional route for electronic contact between Si particles and can participate in lithium storage through alloying and dealloying. When present in the liquid state, Ga may also redistribute as the electrode deforms, potentially helping to maintain contact or reconnect locally separated regions. The design therefore combines polymer-mediated structural support with Ga-mediated conductive contact, providing a basis for examining the electrode morphology, conductivity, and cycling behavior in the following sections.

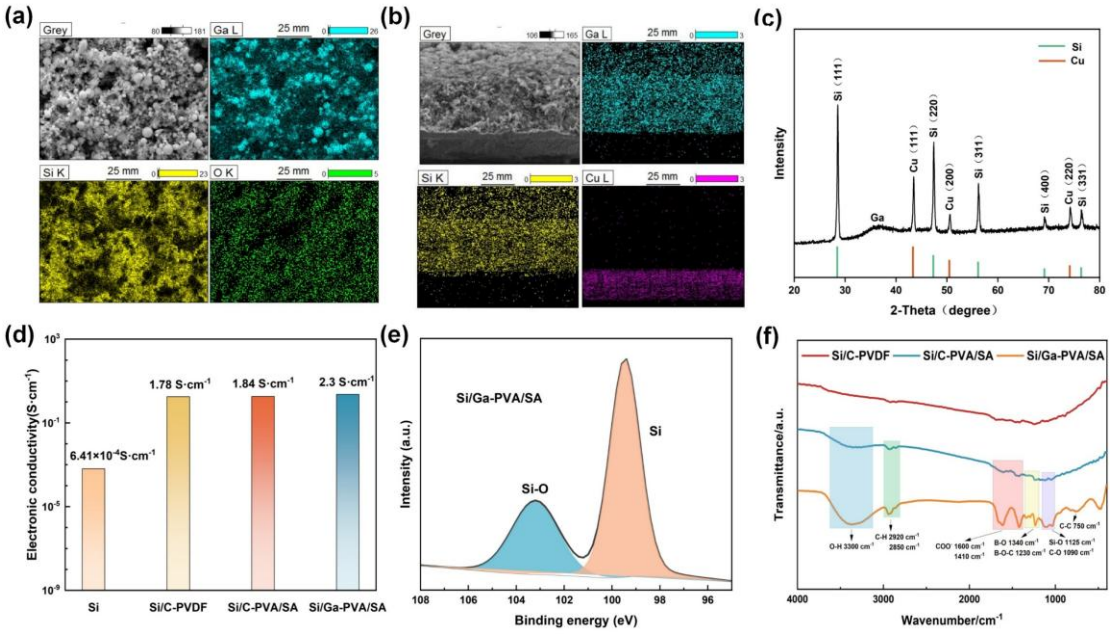

Fig.2 SEM images of the surface (**a**) and cross-section (**b**) of the Si/Ga-PVA/SA anode, along with the corresponding EDS elemental maps; XRD (**c**); comparison of electronic conductivity (**d**); Si 2p XPS spectrum of the Si/Ga-PVA/SA anode (**e**); comparison of FT-IR spectra (**f**)

Top-view field-emission scanning electron microscopy (FESEM) and energy-dispersive X-ray spectroscopy (EDS) mapping were used to examine the morphology and elemental distribution of the Si/Ga–PVA/SA electrode. As shown in Figure 2a, Ga is distributed across the observed surface and intermixed with Si, with no obvious large-

scale segregation in the mapped region. Cross-sectional SEM and EDS mapping further reveal the presence of Ga within the electrode coating (Figure 2b), indicating that its distribution is not restricted to the outer surface. The Ga-on-Si contact-angle measurement in Figure S1 provides complementary information about contact formation between the two components. Together, these observations support the incorporation of Ga throughout the examined regions of the composite coating, providing a morphological basis for evaluating its contribution to electronic contact between Si particles.

The phase composition of the composite electrode was examined by X-ray diffraction (XRD). The Si/Ga–PVA/SA electrode exhibits characteristic reflections associated with Si and the Cu current collector, together with a broad feature near 35° (Figure 2c). The latter is tentatively associated with the Ga-containing phase, although an unambiguous assignment requires comparison with appropriate reference patterns under the relevant measurement conditions[24]. Compared with the pristine Si and Si/C electrodes (Figure S2), the Ga-containing electrode shows no clearly resolved additional reflections attributable to crystalline silicides or other reaction products. These results are consistent with predominantly physical mixing during electrode preparation, while minor or amorphous reaction products remain beyond what can be excluded by the present XRD data.

High-resolution Si 2p X-ray photoelectron spectroscopy (XPS) was subsequently used to examine whether the electrode formulations altered the detectable chemical states of Si. The Si/C–PVDF, Si/C–PVA/SA, and Si/Ga–PVA/SA electrodes exhibit similar spectral features (Figure 2e and Figure S3), with a principal component near 99.8 eV assigned to elemental Si and a higher-binding-energy component around 103.5 eV associated with oxidized Si[25]. No appreciable shift in these components or clearly resolved additional Si chemical state is observed after incorporating Ga or carbon. Combined with the XRD results, the XPS comparison supports the retention of the principal Si chemical states during fabrication and is consistent with a predominantly physically mixed composite, rather than the formation of a readily detectable new Si-containing compound.

The electronic conductivity of the electrode formulations was measured using the four-point probe method (Figure 2d). The pristine nano-Si electrode exhibits a conductivity of 6.41×10^{-4} S cm^{-1}, whereas the Si/C–PVDF and Si/C–PVA/SA electrodes reach 1.78 and 1.84 S cm^{-1}, respectively. Replacing the carbon component with Ga in the PVA/SA-based formulation further increases the measured conductivity to 2.3 S cm^{-1}, approximately 25% higher than that of Si/C–PVA/SA. This comparison demonstrates improved electronic conduction in the Ga-containing formulation. Considered alongside the elemental maps, the result is consistent with Ga contributing to conductive contact within the composite coating. Redistribution of Ga, when liquid, offers a possible means of maintaining such contact during deformation, although this dynamic behavior is not established by the conductivity measurement itself.

Fourier-transform infrared spectroscopy (FTIR) was used to examine the binder-related functional groups and intermolecular interactions (Figure 2f). The two Si/C electrodes exhibit relatively weak polymer-associated signals, potentially reflecting the influence of the carbon-containing matrix on the infrared response. In contrast, the Si/Ga–PVA/SA electrode shows a broad O–H stretching band at 3200–3400 cm^{-1} and C–H stretching bands at 2925 and 2855 cm^{-1}. Bands at 1605 and 1412 cm^{-1} are assigned to the asymmetric and symmetric stretching vibrations of the carboxylate groups in SA, respectively. These features are consistent with the presence of the PVA/SA binder in the composite electrode. The broad O–H band is also compatible with hydrogen-bonded environments involving the hydroxyl and carboxylate groups of the polymers[26]. Additional bands near 1340 and 1230 cm^{-1} are tentatively assigned to B–O and B–O–C vibrations, respectively, consistent with the proposed formation of borate-mediated cross-links[27]. These spectral features support the proposed combination of hydrogen bonding and borate-mediated interactions within the binder, which could contribute to particle cohesion and interfacial adhesion.

Finally, the dispersion stability of the electrode slurry was assessed by visual observation during standing (Figure S4). The Si/Ga–PVA/SA slurry remains macroscopically homogeneous over the displayed observation period, with no obvious sedimentation or solvent separation. This behavior is consistent with the binder matrix

helping to maintain the dispersion of the solid and metallic components before coating. Maintaining this dispersion is relevant to obtaining a uniform coating and limiting composition variations during electrode fabrication.

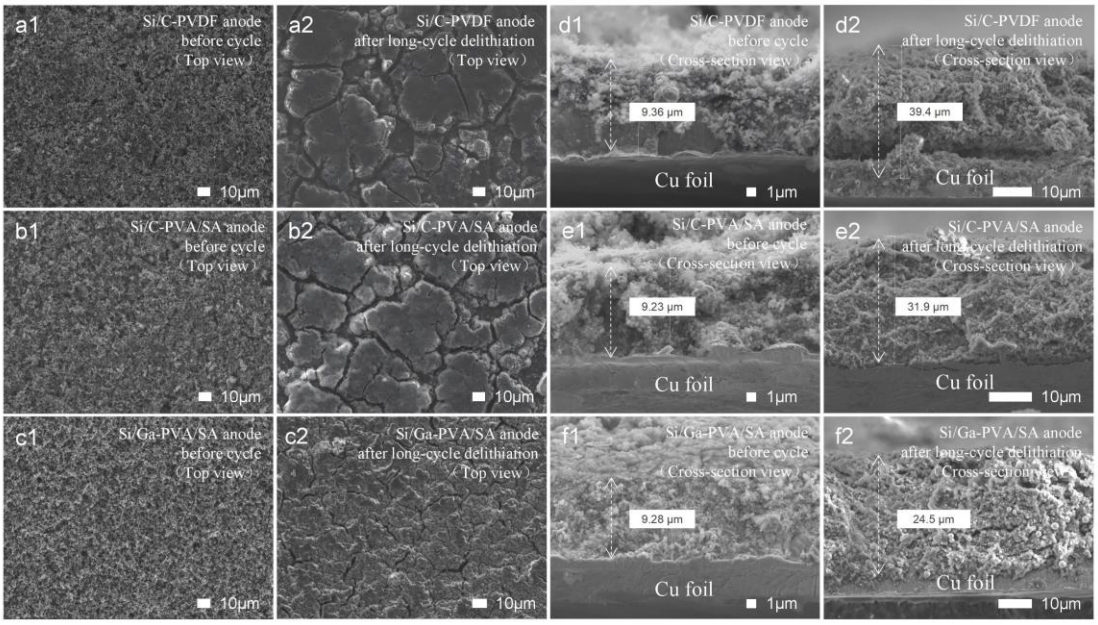

Fig.3 SEM images of the surface (**a1**–**c1**) and cross-section (**d1**–**f1**) of Si/C-PVDF, Si/C-PVA/SA, and Si/Ga-PVA/SA before 200 cycles; SEM images of the surface (**a2**–**c2**) and cross-section (**d2**–**f2**) after 200 cycles

The structural evolution of Si/C–PVDF, Si/C–PVA/SA, and Si/Ga–PVA/SA electrodes was examined by scanning electron microscopy (SEM) before and after 200 galvanostatic cycles within a voltage window of 0.01–1.5 V versus Li^+/Li. Surface and cross-sectional images were compared to assess cracking, coating integrity, and thickness changes associated with repeated lithiation and delithiation. Before cycling, all three electrodes exhibited relatively uniform, densely packed surface morphologies without obvious cracks or localized agglomeration in the observed regions (Figures 3a1–c1). Their initial coating thicknesses were also comparable, at approximately 9–10 μm (Figures 3d1–f1), providing a morphological baseline for evaluating subsequent structural changes.

After 200 cycles, the electrodes exhibited distinct differences in surface integrity. The Si/C–PVDF electrode developed a dense, interconnected crack network, with several cracks extending across the observed field of view (Figure 3d2). This

morphology is consistent with accumulated mechanical damage during repeated Si expansion and contraction. Replacing PVDF with PVA/SA reduced the apparent crack density and connectivity, but widespread cracking remained in the Si/C–PVA/SA electrode (Figure 3b2). The partial improvement is consistent with enhanced adhesion and stress accommodation by the functional polymer binder, although the formulation did not prevent extensive surface damage under the tested conditions. By comparison, the Si/Ga–PVA/SA electrode retained a more continuous surface, with only sparse, relatively narrow, and isolated cracks in the imaged region (Figure 3c2). Thus, replacing the carbon component with Ga while retaining the PVA/SA binder was associated with better preservation of the electrode surface during cycling.

Cross-sectional SEM revealed a corresponding difference in coating expansion and internal integrity. Following 200 cycles and full delithiation, the Si/C–PVDF electrode reached a thickness of 39.4 μm and exhibited pronounced cracks and voids within the coating (Figure 3d2). The Si/C–PVA/SA electrode showed a smaller, but still substantial, thickness increase to approximately 31.9 μm, together with fewer visible cracks and a more cohesive coating structure (Figure 3e2). The Si/Ga–PVA/SA electrode exhibited the smallest final thickness, at 24.5 μm, and retained a comparatively compact cross-section without obvious delamination or major fractures in the observed region (Figure 3f2). Although all three electrodes underwent substantial thickening relative to their initial states, the Ga-containing formulation showed less residual expansion and better preserved coating integrity.

Taken together, the surface and cross-sectional observations indicate improved structural retention in the Si/Ga–PVA/SA electrode under the tested cycling conditions. The comparison between the two carbon-containing electrodes suggests that the PVA/SA binder provides partial stabilization relative to PVDF, while the further improvement observed upon replacing carbon with Ga supports the combined formulation strategy. These trends are consistent with complementary contributions from polymer-mediated cohesion and Ga-mediated maintenance of particle contact, which may help limit crack propagation and coating disruption during cycling. The microscopy results support a formulation-level structural benefit, although they do not

independently establish liquid-state self-healing or a non-additive interaction between Ga and the binder.

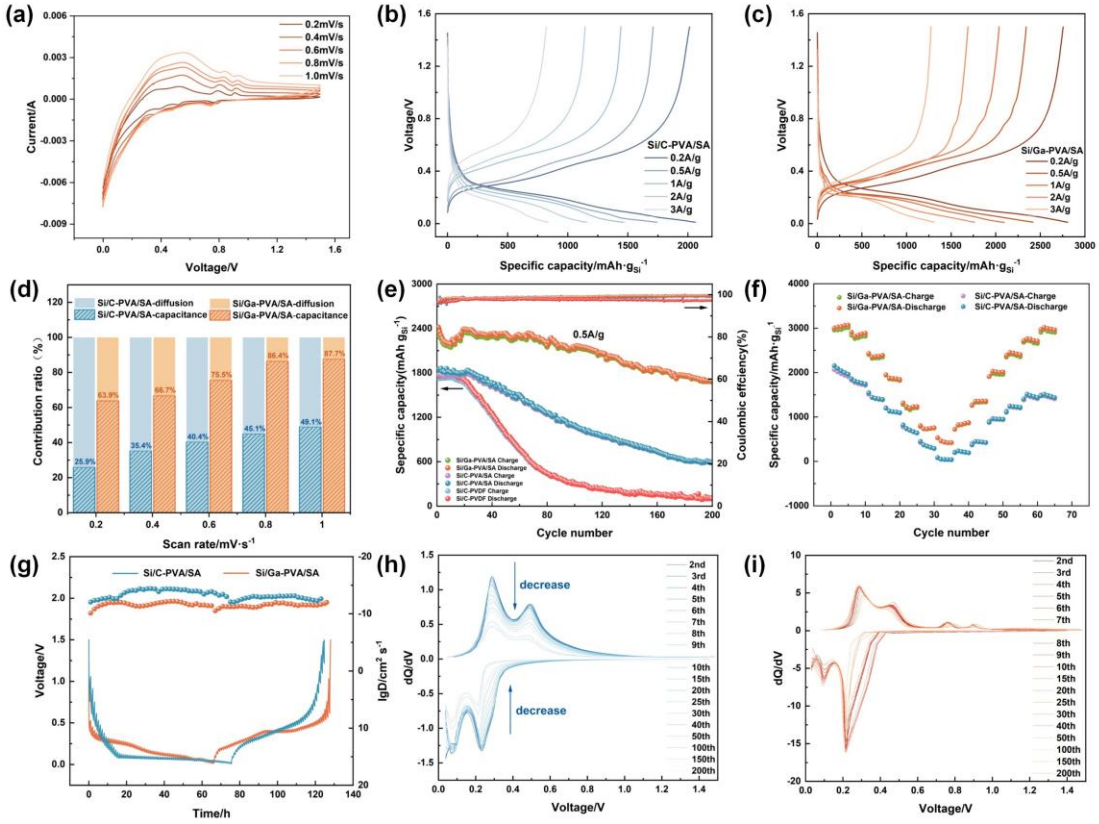

Fig.4 Lithium Storage Performance and Reaction Kinetics. CV curves of Si/Ga-PVA/SA at different scan rates (**a**); constant-current charge-discharge curves of Si/C-PVA/SA (**b**) and Si/Ga-PVA/SA (**c**); Comparison of capacitive and diffusion-controlled contributions for Si/C-PVA/SA and Si/Ga-PVA/SA (**d**); long-term cycling performance of Si/C-PVDF, Si/C-PVA/SA, and Si/Ga-PVA/SA (**e**); and rate capability of Si/C-PVA/SA and Si/Ga-PVA/SA (**f**); GITT voltage distribution during the first cycle (**g**); (**h**) dQ/dV-voltage curves for Si/C-PVA/SA and (**i**) Si/Ga-PVA/SA

The electrochemical performance of Si/Ga–PVA/SA was evaluated against Si/C–PVA/SA to examine the effect of replacing the carbon component with Ga within the same binder system. Si/C–PVDF was additionally included as a reference for the cycling comparison. At 0.5 A g^{-1}, Si/C–PVDF decreased from an initial capacity of 1723.67 mAh g^{-1} to 97.99 mAh g^{-1} after 200 cycles, corresponding to a capacity retention of 5.7% (Figure 4e). Replacing PVDF with PVA/SA improved retention: Si/C–PVA/SA delivered 584.55 mAh g^{-1} after 200 cycles from an initial capacity of 1771.16 mAh g^{-1}, retaining 33.0%. Si/Ga–PVA/SA exhibited the highest retained capacity, decreasing from 2342.25 to 1679.37 mAh g^{-1} over the same cycling period

and retaining 71.7%. These comparisons indicate that the PVA/SA binder provides a partial improvement over PVDF in the carbon-containing electrodes, while replacing carbon with Ga further improves capacity retention under the tested conditions.

Cycling measurements at additional current densities showed that the performance advantage of Si/Ga–PVA/SA extended beyond the 0.5 A g^{-1} condition (Figure S5). The Ga-containing electrode maintained higher capacities than Si/C–PVA/SA at elevated current densities, including 2 and 3 A g^{-1}. At 3 A g^{-1}, its capacity retention exceeded 60% after 200 cycles, with an average Coulombic efficiency above 98%. Together with the post-cycling SEM observations, these results are consistent with better preservation of electrode integrity and electrochemically accessible material in the Ga-containing formulation. They support the combined formulation strategy without independently establishing a self-healing mechanism or a non-additive interaction between Ga and the binder.

The galvanostatic charge–discharge profiles also revealed higher capacities for Si/Ga–PVA/SA across the tested current-density range (Figures 4b and 4c). At the five current densities examined between 0.2 and 3 A g^{-1}, the Ga-containing electrode delivered capacities of 2806.98, 2417.77, 2095.09, 1763.41, and 1310.67 mAh g^{-1}, listed in descending capacity order. The corresponding capacities of Si/C–PVA/SA were 2062.58, 1744.10, 1465.76, 1160.30, and 835.94 mAh g^{-1}. Rate capability was further assessed using a current-density sequence of 0.1 to5 to 0.1 A g^{-1} (Figure 4f). Upon returning to 0.1 A g^{-1}, Si/Ga–PVA/SA showed substantial capacity recovery, whereas Si/C–PVA/SA retained a larger capacity deficit. This difference indicates better tolerance of the imposed rate sequence in the Ga-containing electrode and is consistent with the greater structural retention observed after cycling.

Cyclic voltammetry (CV) was used to examine the electrochemical reactions underlying these performance differences. Measurements were conducted between 0.01 and 1.5 V versus Li^+/Li at scan rates of 0.2, 0.4, 0.6, 0.8, and 1.0 mV s^{-1} for Si/Ga–PVA/SA and Si/C–PVA/SA (Figure 4a and Figure S6). The Ga-containing electrode exhibits cathodic features near 0.03 and 0.21 V, tentatively associated with Si lithiation[28], together with additional reduction peaks near 0.48 and 0.79 V that may

arise from Ga–Li alloying[29]. During the anodic sweep, features near 0.33 and 0.50 V are consistent with the delithiation of Li_xSi, while peaks near 0.85 and 0.90 V are tentatively associated with Li–Ga dealloying. The Si/C–PVA/SA electrode predominantly exhibits the Si-related features[30]. The additional peaks in Si/Ga–PVA/SA therefore support a contribution from Ga-related electrochemical reactions, although identifying the specific phases requires independent phase-sensitive evidence or Ga-only controls.

Differential capacity analysis provided complementary information about the reaction features and their evolution during cycling (Figures 4h and 4i). From the second cycle onward, Si/Ga–PVA/SA exhibits four anodic peaks and two cathodic peaks, whereas Si/C–PVA/SA shows two anodic and two cathodic peaks. The additional features in the Ga-containing electrode are broadly consistent with the CV comparison and suggest that Ga contributes to the total stored charge. Si/Ga–PVA/SA also exhibits more pronounced peaks and sharper shoulders during the initial cycles. Its first lithiation feature begins at approximately 0.21 V, compared with 0.24 V for Si/C–PVA/SA, indicating a difference in the lithiation response without independently establishing a thermodynamic or full-cell energy-density advantage[31].

During prolonged cycling, the differential capacity profiles of Si/Ga–PVA/SA retain comparatively well-defined peak shapes, whereas those of Si/C–PVA/SA show greater peak attenuation and broadening. These changes are consistent with the different capacity-retention trends and suggest better preservation of reaction accessibility in the Ga-containing electrode. The deterioration of the carbon-containing reference may be associated with the loss of electrical contact and active-material isolation accompanying the cracking observed by SEM. Residual capacity fading in Si/Ga–PVA/SA could likewise involve continued interphase growth or partial particle isolation, although the differential capacity profiles alone do not distinguish these contributions.

The scan-rate dependence of selected CV peak currents was examined to assess diffusion-related contributions to the electrochemical response. For both electrodes, the peak current, (ip) varies approximately linearly with the square root of scan rate,

($v^{1/2}$) over the fitted range (Figure S6). The Randles–Sevcik relationship was used as an approximate framework for interpreting this dependence:

$$I_P = \left(2.69 \times 10^5\right) S C n^{1.5} D^{0.5} v^{0.5} \quad (1)$$

Here, *ip* is the peak current in A, *n* is the number of electrons transferred, *S* is the effective electroactive area in cm², *C* is the relevant concentration in mol cm⁻³, *D* is the diffusion coefficient in cm² s⁻¹, and *v* is the scan rate in V s⁻¹[32]. Si/Ga–PVA/SA exhibits a steeper fitted slope than Si/C–PVA/SA, indicating a larger scan-rate-dependent peak response. However, the slope depends on *n*, *S*, and *C*, as well as *D*. Because these parameters are not independently matched between the multiphase electrodes, the slope difference cannot be attributed solely to a higher Li^+ diffusion coefficient. Changes in accessible reaction area, electronic connectivity, and Ga-related charge storage may also contribute[33].

The galvanostatic intermittent titration technique (GITT) was used to estimate an apparent Li^+ diffusion coefficient during the initial charge–discharge cycle (Figure 4g). Under the assumptions of the adopted diffusion model, the coefficient was calculated as

$$D_{Li^+} = \frac{4}{\pi\tau}\left(\frac{n_m V_m}{S}\right)^2 \left(\frac{\Delta E_s}{\Delta E_t}\right)^2 \quad (2)$$

Here, τ is the current-pulse duration, n_m and Vm are the amount and molar volume of the active material, respectively, and *S* is the effective electrode–electrolyte contact area used in the model. ΔE_S denotes the change between relaxed potentials associated with a pulse, and $\Delta E\tau$ is the pulse-induced potential change after correction for the instantaneous ohmic drop[34]. The calculated apparent coefficients span approximately 10^{-12}-10^{-14} cm² s⁻¹ for Si/C–PVA/SA and 10^{-11}-10^{-13} cm² s⁻¹ for Si/Ga–PVA/SA. These ranges suggest different transport responses under the applied protocol. Their quantitative interpretation depends on the pulse and relaxation conditions and on the active-phase, molar-volume, and area assumptions used for the composite electrodes[35].

Electrochemical impedance spectroscopy (EIS) and electrolyte contact-angle measurements further distinguished the interfacial responses of the two formulations.

Si/Ga–PVA/SA exhibits a smaller interfacial impedance arc than Si/C–PVA/SA under the measurement conditions (Figure S7). Its electrolyte contact angle is also lower, at 10.7° compared with 28.3° for the carbon-containing reference (Figure S8), indicating improved electrolyte wetting. Together with the higher measured electronic conductivity of 2.3 S cm^{-1} versus 1.84 S cm^{-1}, these observations identify several factors that may contribute to the improved rate response: better electronic conduction, greater electrolyte wettability, and a smaller interfacial impedance contribution. They provide complementary evidence for altered electrode transport without separately resolving every electronic and ionic process.

The CV data were additionally analyzed using an empirical power-law relationship to compare the scan-rate sensitivity of selected redox peaks:

$$i_p = a v^b \tag{3}$$

which can be expressed in logarithmic form as

$$\log i_p = b \log v + \log a \tag{4}$$

Here, a and b are fitting parameters, with b obtained from the slope of the logarithmic plot. Under idealized conditions, b = 0.5 corresponds to semi-infinite diffusion control, whereas b = 1 describes a response proportional to scan rate, including double-layer charging and some surface-controlled Faradaic processes[36]. The three selected peaks of Si/C–PVA/SA yield b-values of 0.44, 0.64, and 0.67, compared with 0.87, 0.78, and 0.78 for Si/Ga–PVA/SA. The higher values for the Ga-containing electrode indicate a stronger scan-rate-proportional response over the fitted range. The value of 0.44 for the carbon-containing electrode falls below the ideal diffusion-controlled limit, highlighting the need to consider peak selection, non-ideal behavior, and fitting uncertainty when interpreting these exponents[37].

$$i(v) = k_1 v + k_2 v^{1/2} \tag{5}$$

where v denotes electrode potential and k_1 and k_2 are potential-dependent coefficients. Within this empirical decomposition, the k_1 term represents the contribution proportional to scan rate, while the $k_2 v^{1/2}$ term represents the diffusion-related contribution[38]. Si/Ga–PVA/SA exhibits a larger estimated capacitive

fraction than Si/C–PVA/SA across the tested scan rates (Figure 4d). The fraction increases with scan rate and reaches a maximum of 87.7% for Si/Ga–PVA/SA, compared with 49.1% for Si/C–PVA/SA. These results are consistent with the higher *b*-values of the Ga-containing electrode, but the fitted fractions do not exclude bulk alloying or independently establish an intrinsic pseudocapacitive storage mechanism.

Overall, the electrochemical measurements show that the Ga-containing formulation combines improved capacity retention and rate response with higher electronic conductivity, a lower electrolyte contact angle, and distinct interfacial and scan-rate-dependent responses. Considered alongside the post-cycling morphology, these findings are consistent with better preservation of conductive contact and electrochemically accessible material. Ga-related alloying may additionally contribute to the measured capacity. The results therefore support the combined use of Ga and the PVA/SA binder while leaving the specific contributions of dynamic Ga redistribution, binder mechanics, and interphase evolution to be resolved by targeted measurements.

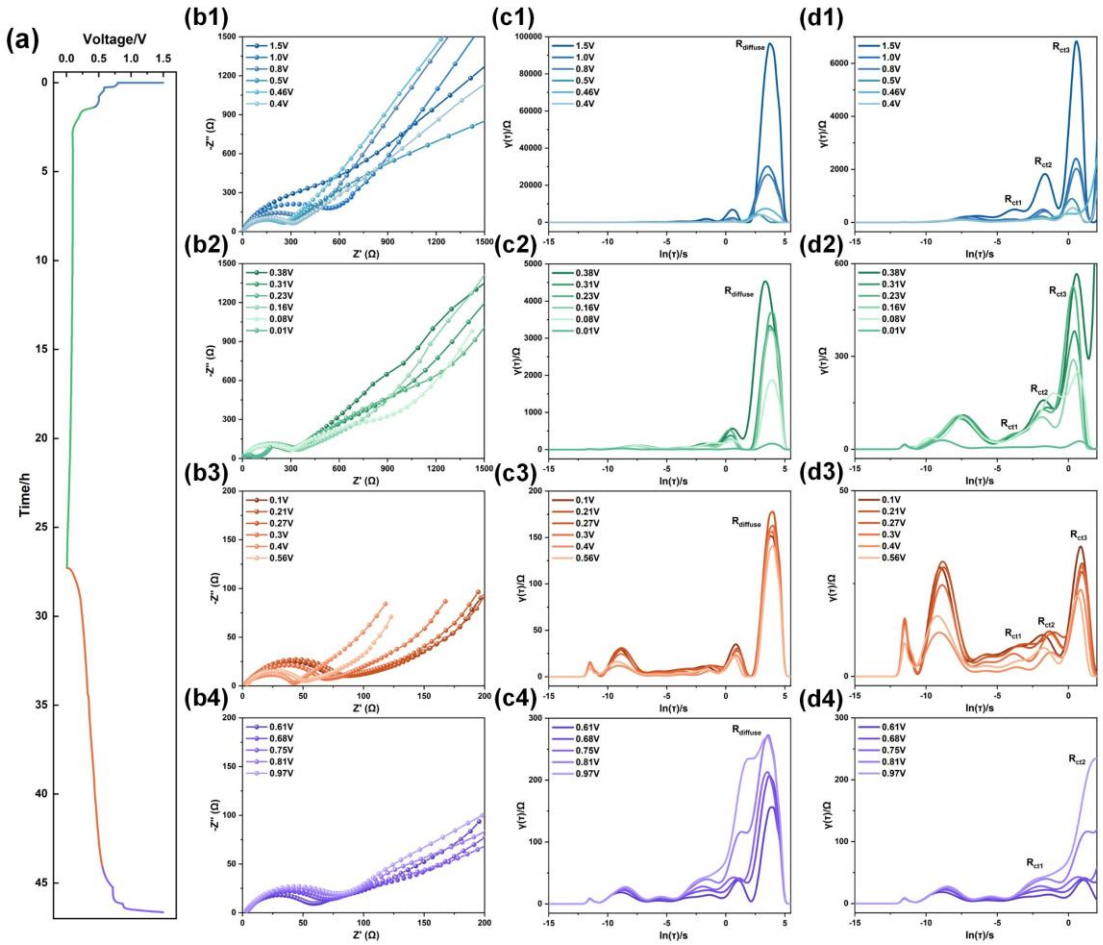

Fig.5 DRT results of Si/Ga–PVA/SA anode. (**a**) Galvanostatic charge/discharge curve of Si/Ga–PVA/SA anode. (**b1-b4**) Ex-situ EIS spectra at different cut-off voltages; (**c1-c4**) corresponding DRT curves;(**d1-d4**) Locally enlarged DRT curves

Potential-dependent electrochemical impedance spectroscopy (EIS) and distribution of relaxation times (DRT) analysis were used to examine the evolution of the Si/Ga–PVA/SA electrode response during lithiation and delithiation. The electrode was cycled at 0.1 A g^{-1} (Figure 5a), and impedance spectra were acquired at selected potentials along the charge–discharge sequence (Figures 5b1–b4). DRT analysis was subsequently applied to distinguish overlapping contributions according to their characteristic relaxation times. Using a normalized relaxation-time distribution, the impedance can be expressed as this equation[39]:

$$Z(\omega)=R_0+R_{pol}\int_{-\infty}^{+\infty}\frac{\gamma(\tau)}{1+j\omega\tau}d\ln\tau \quad (6)$$

where R_0 is the series resistance, R_{pol} is the polarization resistance represented by the distribution, ω is the angular frequency, and j is the imaginary unit. The integration limits refer to the logarithmic relaxation-time coordinate. This representation allows

the impedance response to be examined without prescribing a discrete equivalent circuit, although the recovered distribution depends on the measured frequency range, regularization, and stationarity of the spectra[40].

The resulting distributions exhibit potential-dependent features across four broad relaxation-time ranges. At the shortest times, a minor feature near $\ln(\tau/1s) \approx 12$ shows little variation over the sampled charge–discharge sequence[41]. This feature is distinct from the series resistance R_0, which is represented separately in Equation (6), and its interpretation requires confirmation that it lies within the experimentally resolvable time range. In the adjacent region, approximately $-11.5 < \ln(\tau/1s) < -5$, the response initially decreases during both lithiation and delithiation and subsequently changes only slightly in position and magnitude. This evolution is consistent with a comparatively stable short-time interfacial response over the later sampled potentials. Contributions from the electrode interphase are plausible, but the observed stabilization alone does not identify SEI composition or demonstrate suppression of repeated SEI fracture.

Multiple relaxation features are resolved in the intermediate range of approximately $-5 < \ln(\tau/1s) < 2$. These features may include charge-transfer and coupled interfacial contributions. The components labeled R_{ct1}, R_{ct2}, and R_{ct3} in Figure 5 are discussed using three provisional assignments: a response associated with the SEI/Si interface, a response associated with the SEI/Ga interface, and a contribution related to contact between Ga and Si. These labels provide a framework for interpreting the potential-dependent changes rather than unique identifications of individual physical interfaces. During lithiation, the feature labeled R_{ct3} becomes increasingly prominent as the potential decreases, indicating a redistribution of the intermediate-time impedance response as alloying proceeds.

During delithiation, the intermediate-time features evolve differently. At the later charging potentials, the responses labeled R_{ct1} and R_{ct2} become less distinctly separated and appear to converge into a broader feature, while R_{ct3} remains prominent. These changes are compatible with evolving phase fractions and interfacial contact during dealloying. One possible contribution is the redistribution of regenerated Ga, provided

that it is liquid under the measurement conditions, which could alter its contact with Si and the surrounding interphase. However, the DRT evolution itself does not establish Ga phase recovery or directly demonstrate a liquid-state self-healing process.

At longer relaxation times, $\ln(\tau/1s)>2$, the response labeled R_{diff} may contain diffusion-related and other slow contributions[42]. Its magnitude decreases as lithiation proceeds and increases during delithiation. These trends are consistent with changes in transport pathways accompanying the evolution of lithiated phase fractions and electrode contact. Progressive alloying may modify the accessibility of ion-transport pathways, whereas dealloying may produce a different transport configuration. Because slow responses are particularly sensitive to changes in electrode state during measurement, departures from stationarity must also be considered when interpreting this region.

Taken together, the potential-dependent EIS and DRT results show that the electrode response evolves across several relaxation-time ranges during cycling. The comparatively limited variation of the short-time response contrasts with the more pronounced changes in the intermediate- and long-time regions, suggesting that different interfacial and transport contributions respond differently to lithiation and delithiation. These observations are compatible with the proposed role of Ga in modifying electrode contact and reaction accessibility. Establishing the specific contributions of SEI evolution, Ga redistribution, and bulk diffusion will require correlation with phase-sensitive measurements and appropriate reference electrodes.

3 CONCLUSIONS

In conclusion, a Si/Ga–PVA/SA composite anode was developed by combining Ga with a borax-cross-linked PVA/SA binder to integrate conductive contact with structural support. Under the tested half-cell conditions, the electrode retained a capacity of 1679 mAh g^{-1} after 200 cycles at 0.5 A g^{-1}, corresponding to 71.7% capacity retention, while exhibiting favorable rate response and capacity recovery. Conductivity, impedance, and post-cycling morphological analyses collectively showed improved

electronic conduction, lower interfacial impedance, and reduced residual electrode expansion, consistent with the enhanced cycling stability. These findings support a complementary design in which Ga contributes to conductive contact and the PVA/SA network helps maintain particle cohesion and interfacial adhesion. The specific roles of dynamic Ga redistribution and its interaction with the binder nevertheless require further verification. This study provides experimental support for improving Si anode stability through the combined design of conductive components and functional binders. Further component-controlled studies, cycling at practical areal loadings, and full-cell evaluation are needed to clarify the underlying mechanism and establish the application range.

Supporting Information

Supporting Information is available from XXX.

Notes:

The authors declare no conflict of interest.

Acknowledgments

The work was financially supported by the National Natural Science Foundation of China (22479067), Joint Special Fund for the "Double First-Class" Initiative of Kunming University of Science and Technology (202401BE070001-062), the Yunnan Province Innovation Guidance and Technology-based Enterprise Cultivation Plan (202604CC110035), the Yunnan Province Manufacturing High-Quality Development Special Fund Project (2025ZX002), the Youth Fund of Yunnan Provincial Department of Science and Technology (202501AU070118), Central Guidance for Local Science and Technology Development Fund Project (202507AC040037), and Yunnan Young Talents Program for "Xingdian Talent Support Plan" (KKXX202551007).

Reference

1 Sun L, Liu Y, Wu J *et al.* A Review on Recent Advances for Boosting Initial Coulombic Efficiency of Silicon Anodic Lithium Ion batteries. Small, 2022, 18: 2102894.

2 Gomez-Martin A, Martinez-Fernandez J, Ruttert M *et al.* An electrochemical evaluation of nitrogen-doped carbons as anodes for lithium ion batteries. Carbon, 2020, 164: 261–271.

3 Chang H, Wu Y-R, Han X, Yi T-F. Recent developments in advanced anode materials for

lithium-ion batteries. Energy Mater, 2022, 1: 100003.
4 Rahman MdA, Song G, Bhatt AI, Wong YC, Wen C. Nanostructured Silicon Anodes for High-Performance Lithium-Ion Batteries. Adv Funct Materials, 2016, 26: 647–678.
5 Je M, Han D-Y, Ryu J, Park S. Constructing Pure Si Anodes for Advanced Lithium Batteries. Acc Chem Res, 2023, 56: 2213–2224.
6 Chen Y, Yang L, Guo F *et al.* Mechanical-electrochemical modeling of silicon-graphite composite anode for lithium-ion batteries. Journal of Power Sources, 2022, 527: 231178.
7 Ding J, Li X, Gong L, Tan P. Investigating the failure mechanism of solid electrolyte interphase in silicon particles from an electrochemical-mechanical coupling perspective. Advanced Powder Materials, 2024, 3: 100200.
8 Tang J, Wu F, Dai X *et al.* Robust MXene adding enables the stable interface of silicon anodes for high-performance Li-ion batteries. Chemical Engineering Journal, 2023, 452: 139139.
9 Fu L, Xu A, Song Y *et al.* Pinecone-like Silicon@Carbon Microspheres Covered by Al2O3 nano-petals for lithium-ion battery anode under high temperature. Electrochimica Acta, 2021, 387: 138461.
10 Peng J, Li W, Wu Z *et al.* Si/C composite embedded nano-Si in 3D porous carbon matrix and enwound by conductive CNTs as anode of lithium-ion batteries. Sustainable Materials and Technologies, 2022, 32: e00410.
11 Fox AM, Vrankovic D, Buchmeiser MR. Influence of the Silicon–Carbon Interface on the Structure and Electrochemical Performance of a Phenolic Resin-Derived Si@C Core–Shell Nanocomposite-Based Anode. ACS Appl Mater Interfaces, 2022, 14: 761–770.
12 Jin B, Wang D, Zhu J *et al.* A Self-Healable Polyelectrolyte Binder for Highly Stabilized Sulfur, Silicon, and Silicon Oxides Electrodes. Adv Funct Materials, 2021, 31: 2104433.
13 Gao Y, Qiu X, Wang X *et al.* Chitosan- *g* -Poly(acrylic acid) Copolymer and Its Sodium Salt as Stabilized Aqueous Binders for Silicon Anodes in Lithium-Ion Batteries. ACS Sustainable Chem Eng, 2019, 7: 16274–16283.
14 Wang Y, Yang X, Yuan Y *et al.* N-Rich Solid Electrolyte Interface Constructed In Situ Via a Binder Strategy for Highly Stable Silicon Anode. Adv Funct Materials, 2023, 33: 2301716.
15 Meng J, Li C. Planting CuGa2 seeds assisted with liquid metal for selective wrapping deposition of lithium. Energy Storage Materials, 2021, 37: 466–475.
16 Yu J, Xia J, Guan X *et al.* Self-healing liquid metal confined in carbon nanofibers/carbon nanotubes paper as a free-standing anode for flexible lithium-ion batteries. Electrochimica Acta, 2022, 425: 140721.
17 Liang W, Hong L, Yang H *et al.* Nanovoid Formation and Annihilation in Gallium Nanodroplets under Lithiation–Delithiation Cycling. Nano Lett, 2013, 13: 5212–5217.
18 Zhang H, Bian X, Luo S, Liu C, Hu X. Effect of sodium alginate on the yogurt stability was dependent on the thickening effect and interaction between casein micelles and sodium alginate. International Journal of Biological Macromolecules, 2023, 235: 123887.
19 Li W, Yang S, Chen W *et al.* Free-standing and flexible polyvinyl alcohol-sodium alginate-polypyrrole electrodes based on interpenetrating network hydrogels. Journal of Colloid and Interface Science, 2024, 664: 299–308.
20 Cao P-F, Yang G, Li B *et al.* Rational Design of a Multifunctional Binder for High-Capacity Silicon-Based Anodes. ACS Energy Lett, 2019, 4: 1171–1180.
21 Tang A-L, Zhang L-L, Tan S *et al.* Host-guest synergistic hydrogen bond triggered signal

amplification for visualizing the plant hormone salicylic acid. Chemical Engineering Journal, 2024, 485: 149652.
22 Liu C, Lei F, Li P, Jiang J, Wang K. Borax crosslinked fenugreek galactomannan hydrogel as potential water-retaining agent in agriculture. Carbohydrate Polymers, 2020, 236: 116100.
23 Ma Q, Du L, Yang Y, Wang L. Rheology of film-forming solutions and physical properties of tara gum film reinforced with polyvinyl alcohol (PVA). Food Hydrocolloids, 2017, 63: 677–684.
24 Kim J, Jung J, Park J *et al.* Self-healing Si anodes with robust ionic and electronic conducting network by Ga-In-Sn liquid metal alloy in solid-state batteries. Energy Storage Materials, 2025, 76: 104108.
25 Liu Z, Borodin A, Liu X, Li Y, Endres F. Lithiation of Single-Crystalline Ge(111) and Si(111) Investigated by X-ray Photoelectron Spectroscopy. J Phys Chem C, 2021, 125: 13501–13507.
26 Song Y, Cong Y, Wang B, Zhang N. Applications of Fourier transform infrared spectroscopy to pharmaceutical preparations. Expert Opinion on Drug Delivery, 2020, 17: 551–571.
27 Funakawa H, Miwa K. Synthesis of borate cross-linked rhamnogalacturonan II. Front Plant Sci, 2015, 6.
28 Xu C, Wang Y, Sun S *et al.* Competitive Lithiation Mechanism of Silicon in Aluminum–Silicon Alloy Foil Anodes for Lithium-Ion Batteries. ACS Sustainable Chem Eng, 2024, 12: 17018–17025.
29 Zhou Y, Zhang J, Zhao K *et al.* A novel dual-protection interface based on gallium-lithium alloy enables dendrite-free lithium metal anodes. Energy Storage Materials, 2021, 39: 403–411.
30 Chen JC-M, Yang J, Cheng MM-C. Induced nanoscale roughness of current collectors enhances lithium ion battery performances. Journal of Power Sources, 2019, 430: 169–174.
31 Li J, Wang K, Hu J *et al.* In-situ reconstruction of N-doped carbon nanoflower coating layer for enhancing high pseudo-capacitance in Bi-based fast-charging lithium-ion batteries. Rare Metals, 2025, 44: 1617–1631.
32 Bhushan M, Jha R, Bhardwaj R. Reduced band gap and diffusion controlled spherical n-type ZnS nanoparticles for absorption of UV-Vis region of solar spectrum. Journal of Physics and Chemistry of Solids, 2019, 135: 109021.
33 Geng Z, Chien Y-C, Lacey MJ, Thiringer T, Brandell D. Validity of solid-state Li + diffusion coefficient estimation by electrochemical approaches for lithium-ion batteries. Electrochimica Acta, 2022, 404: 139727.
34 Olsson P-I, Fiandaca G, Maurya PK, Dahlin T, Auken E. Effect of current pulse duration in recovering quantitative induced polarization models from time-domain full-response and integral chargeability data. Geophysical Journal International, 2019, 218: 1739–1747.
35 Juni FJ, Majid SR, Yusuf SNF, Osman Z. Electrochemical characteristics of Cu/Cu2O/C composite electrode for supercapacitor application. Microchemical Journal, 2021, 164: 106055.
36 Kosov AV, Grishenkova OV, Semerikova OL, Isaev VA, Zaikov YP. On the theory of cyclic voltammetry for multiple nucleation and growth: Scan rate influence. Journal of Electroanalytical Chemistry, 2021, 883: 115056.
37 Li J, Wang K, Shi J *et al.* Carbon quantum dot modified W18O49 electrode enables smart energy storage device with a self-diagnosis character. Rare Metals, 2025, 44: 10133–10143.
38 Soleimanzade M, Bahdanchyk M, Hashempour M *et al.* Charging processes of Na4Mn9O18 electrode in aqueous electrolyte. Electrochimica Acta, 2022, 426: 140791.
39 Li J, Wang K, Shi J *et al.* Self-evolving solid electrolyte interphase from Bi2O2CO3 current collector enabling dense electrodeposition for anode-free lithium metal batteries. Energy Storage

Mater, 2026, 89: 105269.
40 Ciucci F, Chen C. Analysis of Electrochemical Impedance Spectroscopy Data Using the Distribution of Relaxation Times: A Bayesian and Hierarchical Bayesian Approach. Electrochimica Acta, 2015, 167: 439–454.
41 Rivera-Sierra G, Ramirez P, Bisquert J, Bou A. Relaxation Time of Multipore Nanofluidic Memristors for Neuromorphic Applications. J Am Chem Soc, 2025, 147: 17529–17538.
42 Sahu A, Singha A, Qureshi M. Interplay of Capacitive and Diffusion Contributions in Redox Active Complex Metal Oxide Rods Channelled into MXene for Improved Charge Transfer Dynamics. ACS Appl Energy Mater, 2024, 7: 6062–6070.

Supplementary Files

This is a list of supplementary files associated with this preprint. Click to download.

- SupportingInformation.docx